

Benchmarking of power control strategies for photovoltaic systems under unbalanced conditions

Allan F. Cupertino^{a,b,*}, Lucas S. Xavier^b, Erick M.S. Brito^b, Victor F. Mendes^b,
Heverton A. Pereira^c

^a Department of Materials Engineering, Federal Center for Technological Education of Minas Gerais, Av. Amazonas, 5253, 30421-169 Belo Horizonte, MG, Brazil

^b Graduate Program in Electrical Engineering – Universidade Federal de Minas Gerais – Av., Antônio Carlos 6627, 31270-901 Belo Horizonte, MG, Brazil

^c Department of Electrical Engineering, Federal University of Viçosa, Av. P. H. Rolfs, s/n, 36570-000 Viçosa, MG, Brazil

ARTICLE INFO

Keywords:

Photovoltaic systems
Unbalanced conditions
Power control strategies
Energy storage requirements
Thermal stress analysis

ABSTRACT

Unbalanced voltage sags are common phenomenon in power systems which affects the performance of grid-connected photovoltaic (PV) systems. The unbalanced voltage conditions results in double-line frequency power oscillations. These oscillations increase the dc-link voltage ripple leading to higher stresses in dc-link capacitors. In this case, the literature presents many power control strategies in order to improve the performance of PV systems during unbalanced conditions. Nevertheless, a deep comparison of these strategies has been missing. This work presents a complete analysis of the main power control strategies proposed in the literature. The energy storage requirements of the converter are analytically deduced and some guidelines for the dc-link design are presented. Furthermore, a case study based on a 11 kW PV system is used to compare the performance of the most interesting strategies in terms of dynamic behaviour, power oscillations and dc-link voltage ripple. Furthermore, the dc-link capacitors stress is discussed, considering the characteristics of reactive power injection, which is required by the modern grid codes. The power losses and the thermal stresses in dc-link capacitors are evaluated and the worst operational scenario is obtained for each power control strategy.

1. Introduction

The grid-connected photovoltaic (PV) systems have experienced a considerable growth in recent years. The interface between the PV array and the distribution system is performed by power converters. These devices are responsible to inject the generated power into the grid and to track the maximum power point of the PV array. Once these devices are grid-connected, they are subjected to voltage disturbances, as unbalances and voltage sags [1].

The voltage sags are a very common phenomenon in the power system. During a voltage disturbance, one or more phase voltages of the power converter are reduced and the currents supplied by the PV system need to be increased to maintain the same amount of injected power. Regarding unbalanced voltage conditions, the negative sequence voltage component in the point of common coupling (PCC) voltage can affect the current control performance, resulting in double-line frequency power oscillations [1–3].

The modern grid codes (GCs) require the low voltage ride-through (LVRT) operation mode. In this case, during a voltage sag, the system

must remains connected to the grid and inject reactive power [4,5]. Depending on the voltage sag depth, some GCs require the injection of a purely reactive current, in order to support the PCC voltage. In such conditions, the generated active power must be reduced in order to guarantee an output current limited to the rated value. Thereby, the PV system must operate in power curtailment mode [6]. Most of GCs require a reactive current profile given by Fig. 1. If V^+ (voltage positive sequence component) is higher than 1 pu, inductive reactive current is provided by the inverter until the maximum voltage limit V_{max} . On the other hand, if the voltage is lower than V_{lim} , capacitive reactive current is provided by the inverter. The droop lines present a slope K . When the voltage is lower than V_{min} , all the capacity of the converter must be used for reactive power injection. Finally, if the voltage is larger than V_{max} , the inverter can be disconnected from the grid. Regarding typical values, $V_{max} = 1.2$ pu, $0.8 \leq V_{lim} \leq 0.9$, $2 \leq K \leq 10$ and $V_{min} = 0.5$ are adopted by the Transmission System Operator (TSO).

Therefore, the following constraints must be fulfilled during an unbalanced voltage sag: injection of reactive power (in agreement with the GC) and the inverter output current must be limited to the rated

* Corresponding author.

E-mail addresses: afcupertino@ieee.org (A.F. Cupertino), lsantx@gmail.com (L.S. Xavier), erickk.brito@gmail.com (E.M.S. Brito), victormendes@cpdee.ufmg.br (V.F. Mendes), heverton.pereira@ufv.br (H.A. Pereira).

<https://doi.org/10.1016/j.ijepes.2018.10.014>

Received 27 April 2018; Received in revised form 2 August 2018; Accepted 11 October 2018

0142-0615/ © 2018 Elsevier Ltd. All rights reserved.

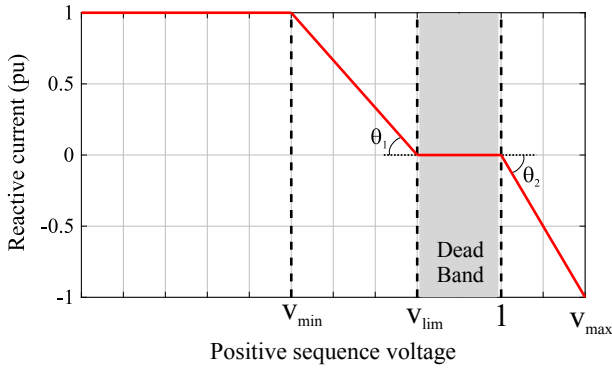


Fig. 1. General reactive current injection curve for modern GCs.

value. Using these constraints, some power control strategies can be employed in order to obtain different performances during voltage sags. For example, only positive sequence currents can be injected, resulting in balanced grid currents. On the other hand, some amount of negative sequence current can be used to cancel out or to reduce the double-line frequency power oscillation [7–9].

Regarding the dc-link, the double-line frequency active power oscillation, leads to dc-link voltage oscillation in the same frequency. Once the low frequency components increase the losses in the dc-link capacitors, this voltage oscillation can affect the lifetime of the dc-link capacitors and consequently the lifetime of the power converter [4,10]. Therefore, the use of negative sequence current components to cancel out the active power oscillation can be an interesting solution to reduce the dc-link capacitor stresses during voltage sags.

In view of the points aforementioned, many works in literature discussed the operation of grid-connected converters during unbalanced conditions, contributing mainly in the following topics: Flexible control strategies during unbalanced conditions [8,7,9]; Dynamic saturation schemes in order to limit the output current [11,12,3]; Control strategies with reduced stress in dc-link capacitors [10,4]. Nevertheless, some gaps can be identified in the technical literature as follows:

- The computation of the dc-link capacitance considering the second order power oscillation is described in some works in literature. Nevertheless, these references generally consider a specific power control strategy, without scrutinize the relationship with the energy storage requirements. In this paper the effect of different power control strategies are presented and compared, and the energy storage requirements are analyzed.
- Since the GCs present different requirements depending on the voltage sag depth, a critical operation condition with respect to the dc-link capacitor stress is expected. Nevertheless, this fact is not approached in the literature.

Therefore, a detailed comparison of the main power control strategies has been missing as well a detailed analysis of the effects of the power control strategies and GC requirements in the dc-link capacitors. The objective of this work is to contribute on these topics, analyzing the main power control strategies proposed in the literature. The contributions of this work are:

- Comparison of the power control strategies in terms of dynamic behaviour, output current quality and ability to cancel out power oscillations;
- Development of analytical expressions for the energy storage requirements of the converter during unbalanced voltage sags as function of the power control strategy employed;
- Discussion of dc-link capacitors stress considering the characteristics of reactive power injection during voltage sags, as required by the

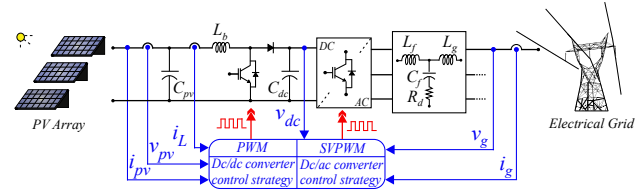


Fig. 2. Schematic of the grid-connected PV system.

modern GCs.

This paper is outlined as follows. Section 2 presents the general control structure of the PV system including the LVRT and power curtailment operation modes. Section 3 presents an overview of the power control strategies discussed in literature and the dynamic saturation scheme employed. Section 4 presents the analytical development of the converter energy storage requirements during unbalanced conditions. The case study based on a 11 kW PV system is presented in Section 5, while the results are presented in Section 6. Finally, the main conclusions are stated in Section 7.

2. System structure and control strategy

2.1. PV inverter topology

The scheme of the three-phase grid-connected PV system studied in this work is illustrated in Fig. 2. As observed, the topology is based on 2 stages. The first one is a dc/dc boost converter which is responsible for tracking the maximum power point of the PV array and reduce the generated power (power curtailment) during voltage sags. The second stage is a 2-level three-phase inverter which is responsible to control the dc-link voltage and inject the generated power into the grid. The dc/ac stage is connected to the grid through a LCL filter in order to attenuate the switching harmonics.

2.2. Dc-ac control strategy

An overview of the complete control strategy is shown in Fig. 3. The dc/ac stage control is based on a **cascade control**. The **outer loop** is responsible for regulating the dc-link voltage. As observed, the square value of dc-link is regulated through a proportional-integral (PI) controller, as presented in [13]. A feedforward of the generated power is considered to improve the dynamic behaviour. Moving average filters (MAV) are included in the dc-link voltage measurement and in the feedforward, since these variables present double line frequency oscillations during unbalanced voltage sags [6,4].

The dc-link voltage loop calculates the reference power P^* . According to the modern GCs, the reactive power reference Q^* is dependent on the positive sequence voltage in the PCC. The current references are computed using the power references and the positive and negative sequence components of the PCC voltage. The analyzed power control strategies are discussed in the next section. Furthermore, the **reference calculator must contain a dynamic saturation scheme in order to maintain the current references below the rated value**. The grid voltage instantaneous symmetric components are computed through a double second order generalized integrator positive and negative sequence extractor (DSOGI-PNSE) [14].

The current control is implemented in stationary ($\alpha\beta$) reference frame. **Adaptive proportional resonant controllers** (PR) are employed to regulate the current references [15]. The current control loops calculate the voltage references which are sent to the space-vector pulse width modulation (SVPWM) algorithm.

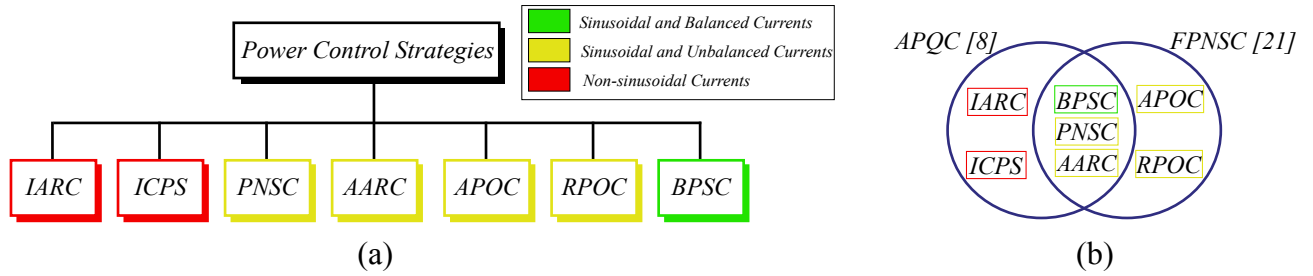


Fig. 5. Overview of the power control techniques: (a) Main power control strategies discussed in literature; (b) Comparison of the flexible control strategies presented by Refs. [8,20].

$$\begin{aligned} v_a &= V^+ \cos(\omega t + \varphi_v^+) + V^- \cos(\omega t + \varphi_v^-), \\ v_b &= V^+ \cos(\omega t + \varphi_v^+ - \frac{2\pi}{3}) + V^- \cos(\omega t + \varphi_v^- + \frac{2\pi}{3}), \\ v_c &= V^+ \cos(\omega t + \varphi_v^+ + \frac{2\pi}{3}) + V^- \cos(\omega t + \varphi_v^- - \frac{2\pi}{3}). \end{aligned} \quad (5)$$

According to the instantaneous power theory [19], any current vector aligned with the voltage vector $\mathbf{v} = [v_a, v_b, v_c]$ results in active power transfer, while any current vector aligned with $\mathbf{v}_\perp = [v_{a\perp}, v_{b\perp}, v_{c\perp}]$ results in reactive power transfer. Then,

$$\begin{aligned} p &= \mathbf{v} \cdot \mathbf{i}^*, \\ q &= \mathbf{v}_\perp \cdot \mathbf{i}^*, \end{aligned} \quad (6)$$

where \mathbf{v}_\perp is a 90° lead version of \mathbf{v} [2,5]. The reference current vector is given by $\mathbf{i}^* = \mathbf{i}_p^* + \mathbf{i}_q^* = [i_a^*, i_b^*, i_c^*]$, where:

$$\begin{aligned} i_a^* &= I^+ \cos(\omega t + \varphi_i^+) + I^- \cos(\omega t + \varphi_i^-), \\ i_b^* &= I^+ \cos(\omega t + \varphi_i^+ - \frac{2\pi}{3}) + I^- \cos(\omega t + \varphi_i^- + \frac{2\pi}{3}), \\ i_c^* &= I^+ \cos(\omega t + \varphi_i^+ + \frac{2\pi}{3}) + I^- \cos(\omega t + \varphi_i^- - \frac{2\pi}{3}). \end{aligned} \quad (7)$$

The power control strategy determines the reference current vector \mathbf{i}^* , which delivers active and reactive power setpoints P^* and Q^* . Depending on the power control strategy adopted, different performances can be reached. Fig. 5 presents an overview of the main power control strategies discussed in the literature. As observed in Fig. 5(a), the power control strategies can be divided into two main groups: Non-sinusoidal and sinusoidal current approaches. Additionally, some flexible strategies have been proposed in [8,20]. These flexible strategies can obtain different performances, as shown in Fig. 5(b). These techniques are described in the next subsections.

3.1. Instantaneous Active Reactive Control (IARC)

The IARC strategy calculates the active and reactive reference current vectors as [7]:

$$\begin{aligned} \mathbf{i}_p^* &= \frac{P^*}{|\mathbf{v}|^2} \mathbf{v}, \\ \mathbf{i}_q^* &= \frac{Q^*}{|\mathbf{v}|^2} \mathbf{v}_\perp, \end{aligned} \quad (8)$$

where $|\mathbf{v}|$ is the module of the three phase vector \mathbf{v} , given by:

$$|\mathbf{v}|^2 = (V^+)^2 + (V^-)^2 + 2V^+V^- \cos(2\omega t + \varphi_v^+ - \varphi_v^-). \quad (9)$$

When IARC strategy is employed, the instantaneous active and reactive power delivered to the grid are constant. Therefore, in theory, no oscillating active and reactive power are delivered to the grid [7]. Nevertheless, when negative sequence components are present in the grid voltage, the resulting reference currents are not sinusoidal. According to [8], the theoretical total harmonic distortion of output current when only active power is injected can be estimated by:

$$THD_i = \frac{u}{\sqrt{1-u^2}}, \quad (10)$$

where u is the unbalanced voltage factor, given by:

$$u = \frac{V^-}{V^+}. \quad (11)$$

This issue is a serious drawback of the IARC strategy. The distorted reference currents require the implementation of more complex control system, as proportional multi-resonant controllers [7]. Additionally, the distorted current waveforms can increase the power losses in the output filter inductors. Finally, the dynamic current saturation scheme becomes complex when distorted currents are considered.

3.2. Instantaneously Controlled Positive-Sequence (ICPS)

The ICPS is discussed in [7,8]. This technique was developed considering only active power injection. In fact, the instantaneous active power delivered can be calculated by:

$$p = \mathbf{v} \cdot \mathbf{i}^* = \mathbf{v} \cdot \mathbf{i}^+ + \mathbf{v} \cdot \mathbf{i}^-. \quad (12)$$

For ICPS, the objective is to inject a constant instantaneous active power employing only the positive sequence currents [7,8]. Therefore, the following constraints are imposed to the current vector:

$$\begin{aligned} \mathbf{v} \cdot \mathbf{i}^+ &= P, \\ \mathbf{v} \cdot \mathbf{i}^- &= 0. \end{aligned} \quad (13)$$

Therefore, $\mathbf{i}^- = 0$ and the current reference $\mathbf{i}^* = \mathbf{i}_p^*$ can be computed by [7]:

$$\mathbf{i}_p^* = \frac{P^*}{(V^+)^2 + V^+V^- \cos(2\omega t + \varphi_v^+ - \varphi_v^-)} \mathbf{v}^+. \quad (14)$$

According to [8], the theoretical output current THD for ICPS can be estimated by:

$$THD_i = \sqrt{\frac{u^2}{2\sqrt{1-u^2}(1-\sqrt{1-u^2})}} - 1, \quad (15)$$

Although the current reference for ICPS presents harmonics, this technique results in a smaller THD than IARC strategy. Nevertheless, when ICPS is employed only the oscillating component of the active power is cancelled. Furthermore, this technique cancels the oscillation of active power only if $Q^* = 0$. Thereby, this technique can be suitable during unbalanced voltage operation but not during unbalanced voltage sags, when the grid codes generally require reactive power support.

3.3. Positive and Negative Sequence Control (PNSC)

In order to determine the expressions for the reference currents generated by the PNSC strategy, it is initially assumed that only active power is delivered to the grid. Moreover, it is imposed as a condition that the delivered active power is free of oscillations. Considering these constraints, the reference for active and reactive currents vector are given by [7,8]:

Table 1

Power control strategies previously presented from the FPNSC perspective.

Strategy	PNSC	AARC	BPSC	APOC	RPOC
k_1	$\frac{1}{1-u^2}$	$\frac{1}{1+u^2}$	1	$\frac{1}{1-u^2}$	$\frac{1}{1+u^2}$
k_2	$\frac{1}{1-u^2}$	$\frac{1}{1+u^2}$	1	$\frac{1}{1+u^2}$	$\frac{1}{1-u^2}$

$$\begin{aligned} \mathbf{i}_p^* &= \frac{P^*}{(V^+)^2 - (V^-)^2} \mathbf{v}^+ - \frac{P^*}{(V^+)^2 - (V^-)^2} \mathbf{v}^-, \\ \mathbf{i}_q^* &= \frac{Q^*}{(V^+)^2 - (V^-)^2} \mathbf{v}_\perp^+ - \frac{Q^*}{(V^+)^2 - (V^-)^2} \mathbf{v}_\perp^-. \end{aligned} \quad (16)$$

When PNSC strategy is employed, the instantaneous active power oscillation can be canceled only if the reactive power reference is null. Therefore, it presents the same drawback of ICPS for reactive power injection. As advantage of previous strategies, PNSC results in sinusoidal currents into the grid.

3.4. Average Active-Reactive Control (AARC)

In AARC strategy, the current reference is computed as follows [7,8]:

$$\begin{aligned} \mathbf{i}_p^* &= \frac{P^*}{(V^+)^2 + (V^-)^2} \mathbf{v}^+ - \frac{P^*}{(V^+)^2 + (V^-)^2} \mathbf{v}^-, \\ \mathbf{i}_q^* &= \frac{Q^*}{(V^+)^2 + (V^-)^2} \mathbf{v}_\perp^+ - \frac{Q^*}{(V^+)^2 + (V^-)^2} \mathbf{v}_\perp^-. \end{aligned} \quad (17)$$

When AARC is employed, the output current becomes sinusoidal. For a given grid voltage vector \mathbf{v} , the current references computed through AARC results in the smallest possible collective rms value which delivers the references P^* and Q^* over one grid period [2]. Therefore, the AARC strategy results in the lower conduction losses in the system and higher efficiency.

Finally, AARC is able to cancel oscillations of active power only if the active power reference is null. Therefore, this technique is interesting for grid connected PV systems only if the voltage sag reaches a condition which the grid code requires only reactive power injection.

3.5. Balanced Positive-Sequence Control (BPSC)

The current references for BPSC strategy are computed as [7,8]:

$$\begin{aligned} \mathbf{i}_p^* &= \frac{P^*}{(V^+)^2} \mathbf{v}^+, \\ \mathbf{i}_q^* &= \frac{Q^*}{(V^+)^2} \mathbf{v}_\perp^+. \end{aligned} \quad (18)$$

In the BPSC, both instantaneous active and reactive powers will be affected by oscillations under unbalanced grid conditions. The null value in P^* or Q^* setpoints do not cancel any power oscillation, which is a difference from the previous strategies. On the other hand, this method is the only one that permits sinusoidal and balanced currents in the power system.

3.6. Flexible power control strategies

The discussed power control strategies present different performances and characteristics. Depending on the situation, one strategy is more advantageous than others. Therefore, a more general formulation which becomes the previous strategies particular cases is very attractive in the control point of view.

Ref. [8] proposes a flexible power control strategy when only active power injection is considered. This method, called in this paper as adjustable power quality control (APQC) computes the current reference using two power performance parameters, α and β . The value of these variables define the performance. Five strategies are obtained, as illustrated in Fig. 5(b). The APQC strategy is based on an algorithm which calculates the power performance parameters as function of the

maximum accepted THD and power oscillation. Nevertheless, this strategy is few attractive since it does not consider reactive power injection and it also can result in distorted currents.

On the other hand, reference [20] discuss the flexible positive and negative sequence control (FPNSC). In this strategy, the current reference vector is computed as:

$$\begin{aligned} \mathbf{i}_p^* &= k_1 \frac{P^*}{(V^+)^2} \mathbf{v}^+ + \left(1 - k_1\right) \frac{P^*}{(V^-)^2} \mathbf{v}^-, \\ \mathbf{i}_q^* &= k_2 \frac{Q^*}{(V^+)^2} \mathbf{v}_\perp^+ + \left(1 - k_2\right) \frac{Q^*}{(V^-)^2} \mathbf{v}_\perp^-. \end{aligned} \quad (19)$$

where k_1 and k_2 are positive numbers which can be selected to obtain different performances. A similar approach is also discussed in [9]. FPNSC presents the advantage to compute only sinusoidal currents. Additionally to the previous power control strategies, the FPNSC can derive 2 other interesting strategies: the active power oscillation cancellation (APOC) and the reactive power oscillation cancellation (RPOC). In these strategies, the instantaneous oscillating power cancellation is reached for any operating power factor [4].

The previous power control strategies can be obtained from FPNSC employing the values of k_1 and k_2 shown in Table 1. As observed, only positive sequence current is injected in BPSC, since $k_p = k_q = 1$. In other cases, the performance parameters are calculated as function of the unbalance factor u . Intermediate performances can be reached if other values of k_1 e k_2 are chosen.

Once FPNSC results in sinusoidal currents, a current dynamic saturation scheme can be derived [11]. In the case of PV systems, the active power limitation is preferred since the grid codes require reactive power injection during voltage sags. The maximum active power which can be injected without exceed the current limit I_{max} is given by [3]:

$$P = \frac{-2xQ^* + \sqrt{y(3I_{max}uV^+)^2 - (2zQ^*)^2}}{2y}, \quad (20)$$

where

$$x = (k_1 + k_2 - 2k_1k_2)u\sin(\theta), \quad (21)$$

$$y = k_1^2[1 - 2u\cos(\theta) + u^2] - 2k_1[1 - u\cos(\theta)] + 1, \quad (22)$$

$$z = k_1[1 - u\cos(\theta)] + k_2[1 + u\cos(\theta)] + k_1k_2[u^2 - 1] - 1, \quad (23)$$

$$\theta = \left\{ \varphi_v^+ - \varphi_v^-, \varphi_v^+ - \varphi_v^-, \frac{2\pi}{3}, \varphi_v^+ - \varphi_v^-, \frac{2\pi}{3} \right\}. \quad (24)$$

As observed, the power limit needs to be evaluated for the three values of θ , since the most stressed phase saturates the active power transfer. Therefore, the active power limit is then calculated by [3]:

$$P_{max} = \min\{P_a, P_b, P_c\}. \quad (25)$$

Finally, this power limit is used as reference for the power curtailment strategy, as discussed in Section 2. Due to its interesting characteristics, FPNSC is addressed in this work.

4. Energy storage requirements during unbalanced conditions

The active power oscillations derived from unbalanced voltage conditions affects the inverter dc-link voltage. The objective of this section is to analyze this mechanism and give some guidelines for dc-link capacitance design. An energy approach is considered in this work. The harmonics generated by the converter switching are neglected in this analysis.

The dc-link capacitance can be calculated by:

$$C = \frac{2E_{nom}}{v_{dc}^2}, \quad (26)$$

where v_{dc} is the dc-link voltage and E_{nom} is the minimum value of the

nominal energy storage, which is given by:

$$E_{nom} = \frac{\Delta E}{k_{max}^2 - 1}. \quad (27)$$

where k_{max} is introduced to relate the energy variation due to the difference between nominal and maximum voltage. In order to complete the design methodology, the energy variation ΔE must be known.

The energy variation can be obtained by:

$$\Delta E = \max(\tilde{e}_{cap}), \quad (28)$$

where \tilde{e}_{cap} is the instantaneous energy variation in the capacitor which can be obtained as:

$$\tilde{e}_{cap}(t) = \int \tilde{p}(t) dt. \quad (29)$$

On the other hand, the power flow analysis in dc-link leads to the following relation:

$$\tilde{p} = v_{dc} i_c = C v_{dc} \frac{dv_{dc}}{dt} \approx C v_{dc}^* \frac{dv_{dc}}{dt}, \quad (30)$$

where $v_{dc} \approx v_{dc}^*$ is assumed. In such conditions, the dc-link voltage can be approximated by:

$$v_{dc}(t) \approx v_{dc}^* + \frac{1}{C v_{dc}^*} \int \tilde{p} dt. \quad (31)$$

Therefore, the dc-link voltage ripple can be approximated by:

$$\Delta v_{dc} = (k_{max} - 1) v_{dc}^* \approx \frac{\Delta E}{2 C v_{dc}^*}. \quad (32)$$

As observed, the maximum dc-link voltage ripple is approximately proportional to the energy variation. In the following steps, expressions for the energy storage requirements are derived. The use of relations (5)–(7) results in:

$$\begin{aligned} \tilde{p}(t) = & \frac{3}{2} V^+ I^- \cos \left(\overbrace{2\omega t + \varphi_v^+ + \varphi_i^-}^{\delta^\pm} \right) \\ & + \frac{3}{2} V^- I^+ \cos \left(\overbrace{2\omega t + \varphi_v^- + \varphi_i^+}^{\delta^\mp} \right) \end{aligned} \quad (33)$$

This expression shows the instantaneous active power oscillation for arbitrary voltage and current with positive and negative sequences. Substituting (33) in (29):

$$\tilde{e}_{cap}(t) = \frac{3}{4} \frac{V^+ I^+}{\omega} \left[\frac{I^-}{I^+} \sin \delta^\pm + \frac{V^-}{V^+} \sin \delta^\mp \right] \quad (34)$$

The energy in the dc-link changes according to a second order sinusoidal function, which generates double line frequency ripple. If the two sinusoidal terms of (34) cancels each other, in theory no oscillating active power and no dc-link voltage oscillation are observed.

In fact, the current and voltage unbalance factor are not independent, since they are coupled through the power control strategy. The same can be concluded for the voltage and current angles. In order to determine the relation between these variables, a fasorial approach is considered. Using (19), it is possible to write:

$$\frac{I^- \angle \varphi_i^-}{I^+ \angle \varphi_i^+} = \frac{(1-k_1) \frac{P^*}{V^-} \angle \varphi_v^-}{k_1 \frac{P^*}{V^+} \angle \varphi_v^+} + \frac{(1-k_2) \frac{Q^*}{V^-} \angle \varphi_v^- - \frac{\pi}{2}}{k_2 \frac{Q^*}{V^+} \angle \varphi_v^+ + \frac{\pi}{2}}. \quad (35)$$

Developing (35), it is possible to obtain:

$$\frac{I^-}{I^+} = \frac{V^+}{V^-} \sqrt{\frac{[(1-k_1)P^*]^2 + (1-k_2)Q^*^2}{[k_1 P^*]^2 + [k_2 Q^*]^2}}, \quad (36)$$

$$\delta^\pm = \delta^\mp + \zeta - \tan^{-1} \left(\frac{1-k_2}{1-k_1} \frac{Q^*}{P^*} \right) - \tan^{-1} \left(\frac{k_2}{k_1} \frac{Q^*}{P^*} \right), \quad (37)$$

where ζ is included to guarantee the correct angle estimation when $1-k_1 < 0$ ¹. This variable is given by:

$$\zeta = \begin{cases} 0, & \text{if } 1-k_1 \geq 0 \\ \pi, & \text{if } 1-k_1 < 0. \end{cases} \quad (38)$$

The Eqs. (34), (36) and (37) compute the theoretical value of the second harmonic oscillating components in dc-link storage energy. The different power control strategies with sinusoidal currents can be easily analyzed using this general model and the parameters of Table 1. The simplifications obtained are summarized in Table 2. Using these simplifications, the energy variation can be compute when the ratio Q^*/P^* is changed. The obtained performance is presented in Fig. 6. Based on these theoretical results, the following conclusions can be stated:

- The maximum energy storage variation ΔE is function of the V^- , I^+ , ω and also the control strategy employed;
- The BPSC strategy results in dc-link energy variation equal to $\Delta E = \frac{3V^- I^+}{4\omega}$. Furthermore, the ratio Q^*/P^* does not have influence in this technique;
- When PNSC or AARC strategies are employed, the maximum energy storage variation is very sensible to the ratio Q^*/P^* . When $Q^* = 0$, PNSC results in no second order component in the dc-link voltage. The ripple is generated only by the switching components which are not included in the mathematical modeling. On the other hand, when $P^* = 0$, AARC results in no second order component in the dc-link voltage. Nevertheless, both strategies can derive larger energy variation than BPSC strategy. In the worst case, the obtained energy variation is two times larger;
- When APOC or RPOC strategies are employed, the dependency of the power factor is eliminated. In this case, APOC results in no second order component in the dc-link voltage while RPOC results in oscillations with the double amplitude of BPSC strategy.

In view of these facts, the use of PNSC and RPOC strategies are less interesting due to the larger impact in the converter dc-link. Therefore, BPSC and APOC seems to be more interesting strategies for grid connected PV systems and will be further compared in the case studies of this work. Although AARC can present a larger impact in dc-link voltage, the lower conduction losses in the system are a positive feature. Therefore, this strategy is also addressed.

In order to determine the energy storage requirements for different rated power, the energy requirements are defined per unit (pu). The worst case of energy variation is assumed ($\Delta E = \frac{3V^- I^+}{2\omega}$). In this case:

$$W_{conv} = \frac{E_{nom}}{S_n} = \frac{V^-}{V_n} \frac{I^+}{I_n} \frac{1}{\omega (k_{max}^2 - 1)}, \quad (39)$$

where W_{conv} is the energy storage requirement of the converter. According to [21], the values employed in commercial 2-level converters are in the range of 2 and 4 J/kVA. Fig. 7 presents the behaviour of W_{conv} as function of V^- and I^+ varying from 0 to 1 pu. In this study, $k_{max} = 1.1$ and $\omega = 377 \text{ rad/s}$ are assumed. As observed, when the negative sequence voltage is smaller than 0.3 pu, the value of 4 J/kVA satisfy the 10 % of voltage ripple requirement.

The modelling presented in this section is useful for the dc-link capacitance design. Basically, the minimum energy storage requirement W_{conv} can be obtained from Eq. (39) considering 1 pu of positive sequence current and the maximum negative sequence voltage. The obtained value must be multiplied by the converter rated power resulting

¹ In fact, the function $\tan^{-1}(x)$ is defined in the interval $(-\frac{\pi}{2}, \frac{\pi}{2})$. Thereby, if $1-k_1 < 0$, the inversion interval must be changed. When the variable ζ is included, the correct computation of the angles is guaranteed.

Table 2

Simplifications in the energy storage function when the strategies of Table 1 are considered.

Strategy	PNSC	AARC	BPSC	APOC	RPOC
Eq. (36)	$\frac{I^-}{I^+} = u$	$\frac{I^-}{I^+} = u$	$\frac{I^-}{I^+} = 0$	$\frac{I^-}{I^+} = u$	$\frac{I^-}{I^+} = u$
Eq. (37)	$\zeta = \pi$	$\zeta = 0$	$\zeta = 0$	$\delta^\pm = \delta^\mp + \pi$	$\delta^\pm = \delta^\mp$

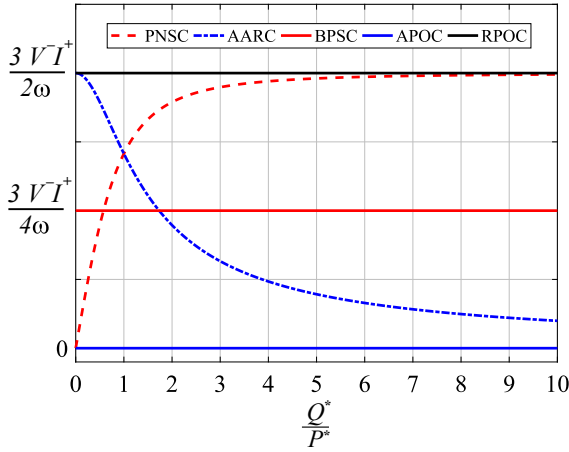


Fig. 6. Comparison of the maximum energy storage variation with the ratio $\frac{Q^*}{P^*}$ for the discussed power control strategies.

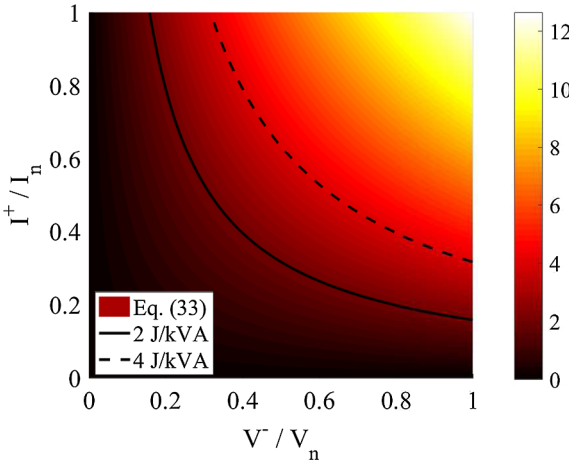


Fig. 7. Comparison between the energy storage requirements and the typical values employed.

in the energy storage E_{nom} . Finally, using the dc-link voltage and E_{nom} , the minimum dc-link capacitance is computed through Eq. (26).

5. Case study

The case study parameters are presented in Table 3. The value of dc-link capacitor is defined within the range employed in most commercial inverters. The value of dc-link voltage is defined based on the voltage drop caused by the passive filter and for a maximum grid voltage of 1.2 pu.

The parameters of the controllers are presented in Table 4. All controllers are implemented using a sampling frequency equal to the switching frequency. For PI compensator, the Tustin method is employed. For resonant controllers, the Tustin method with pre-warping is used. All simulations were implemented in PLECS environment.

Table 3

Parameters of the simulated system.

Parameter	Value
Grid voltage (line to line) (v_g)	380 V
Rated power (S_n)	11 kVA
Inverter switching frequency f_s	12 kHz
Inverter maximum current peak value I_{max}	23.6 A
LCL filter inductance ($L_f = L_g$)	0.5 mH
LCL filter inductance X/R ratio ^a	7.65
LCL filter capacitance (C_f)	6 μF
Damping resistor R_d	100 m Ω
Dc-link Voltage (v_{dc})	750 V
Dc-link capacitance C_{dc}	220 μF (3.85 J/kVA)
Boost converter inductance	1.2 mH
Boost converter inductor resistance	35 m Ω
Boost converter capacitance (C_{pv})	135 μF
Boost converter switching frequency f_{sb}	20 kHz
PV array maximum power ^b P_{mpp}	9.75 kW
Maximum power point voltage ^b V_{mpp}	406.77 V

^a X/R ratio is calculated for 60 Hz.

^b Under standard conditions ($G = 1000 \text{ W/m}^2$, $T_c = 25^\circ \text{C}$).

Table 4

Parameters of the controllers.

Parameter	Value
Dc-link control: Proportional Gain	0.023
Dc-link control: Integral Gain	0.39
Grid current control: Proportional Gain	7.42
Grid current control: Resonant Gain	2000
Boost input voltage control: Proportional Gain	0.17
Boost input voltage control: Integral Gain	76.31
Boost current control: Proportional Gain	0.02
Boost current control: Integral Gain	0.84
Moving average filter frequency	120 Hz
MPPT Sampling frequency	20 Hz
MPPT Voltage increment	0.5 V

Three power control strategies are evaluated: BPSC, AARC and APOC. The results are divided in three parts. Firstly, the dynamic behaviour is evaluated during an unbalanced voltage sag. The performance of the current dynamic saturation and the power curtailment strategy is discussed.

Secondly, the capacitor voltage ripple is evaluated for different unbalance factors. The value obtained in the simulations is compared with the analytical results derived in Section 4. Additionally, the MPPT instantaneous efficiency is also computed for each strategy as follows:

$$\eta_{mppt}(t) = 100 \frac{p_{pv}(t)}{p_{pv}^*(t)} (\%), \quad (40)$$

where $p_{pv}^*(t)$ is the available power in the PV array and $p_{pv}(t)$ is the power extracted by the maximum power point algorithm.

Once the dynamic saturation scheme guarantees that the converter current is below the rated value, the thermal stresses in the power semiconductors and passive filter elements will not increase significantly during unbalanced conditions. Nevertheless, the second order harmonic component in the capacitor current can increase the thermal stress and affect the lifetime of dc-link and solar array capacitors. Therefore, the power losses and the thermal stresses in these capacitors are evaluated.

The capacitor power loss considers the ohmic losses in equivalent series resistance (ESR). Once ESR is not constant with frequency, different losses contributions are observed for the doubled line frequency and the switching components. Therefore, the method proposed by [22] is employed to obtain the power losses and the temperature of the capacitors. Basically, the power losses are computed for each frequency

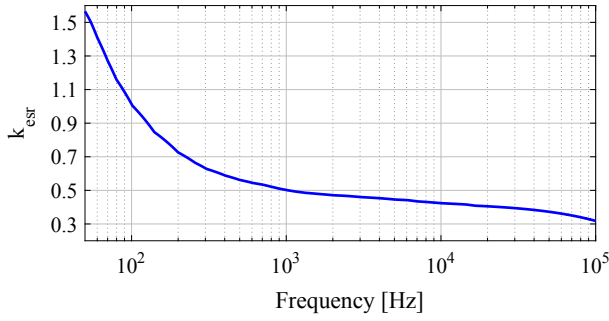


Fig. 8. Correction factor k_{esr} as function of the frequency.

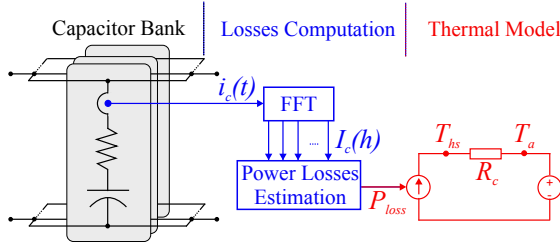


Fig. 9. Complete block diagram of the capacitor stress analysis.

component of the capacitor current. The value of ESR is corrected for each frequency component using the correction factor k_{esr} which is provided by the manufactures. Fig. 8 presents the behaviour of k_{esr} for snap-in electrolyte capacitors. The hot-spot temperature is estimated through the thermal resistance R_c and the ambient temperature T_a . The complete block diagram of the capacitor stress analysis is presented in Fig. 9.

The first step in the dc-link design procedure is define the technology of the capacitors. For example, the traditional electrolyte capacitors are an interesting solution in terms of initial costs but present reduced useful life. On the other hand, high density film capacitors is an emerging solution which presents a higher useful life. Although this solution is interesting from the reliability point of view, it increases the initial costs of the inverter [22]. In this work, electrolyte capacitors are employed. The physical design of the dc-link and solar array capacitors is based on the following guidelines:

- The individual capacitor voltage cannot be larger than 90 % of capacitor rated voltage. Series connection can be employed to attend this requirement;
- The capacitor hot-spot temperature cannot exceed the rated value specified by the manufacturer. In this case, the parallel connection can be employed to decrease current and the losses per capacitor. Consequently, the hot-spot temperatures can be reduced.

In this work, the hot-spot temperature is estimated considering a maximum ambient temperature of 40 °C. The losses are estimated considering the harmonic components until 100 kHz which are the most

Table 5
Parameters for losses evaluation.

Parameter	C_{pv}	C_{dc}
Part Number	B43630E2277M0	B43630A9227M0
Manufacturer	Epcos	Epcos
Rated Voltage	250 V	450 V
Rated Capacitance	270 μ F	220 μ F
ESR per Cap. (100 Hz)	310 m Ω	470 m Ω
Number of Cap.	2 (2×1)	4 (2×2)
Thermal Resistance	2.3 °C/W	2.3 °C/W

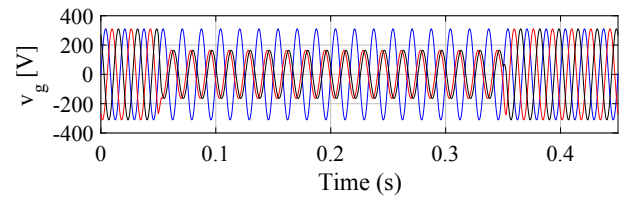


Fig. 10. Voltage profile in PCC.

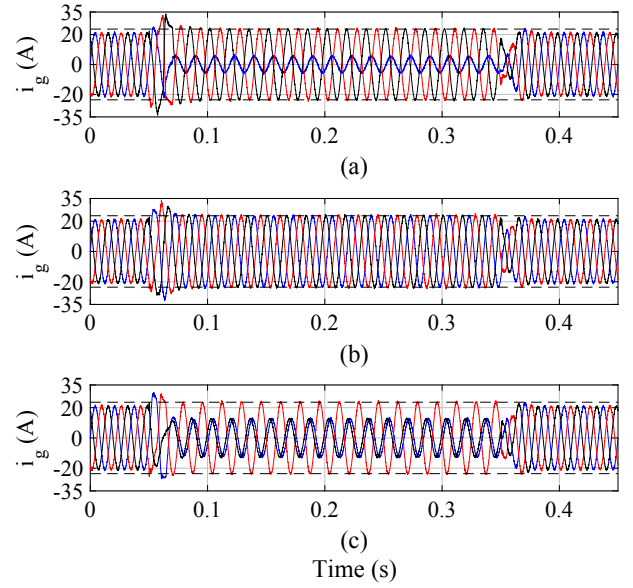


Fig. 11. Dynamic behaviour of the grid current for the approached power control strategies: (a) APOC; (b) BPSC; (c) AARC.

significant for losses analysis. The parameters of the designed capacitor banks are presented in Table 5.

6. Results

6.1. Dynamic behaviour

The dynamic behaviour of the power control strategies are compared using the unbalanced voltage sag scenario presented in Fig. 10. This voltage sag contains 0.6 pu of positive sequence and 0.4 pu of negative sequence with $\varphi_v^+ = \varphi_v^- = 0$. This study also considers the PV array generating the nominal power. When the positive sequence voltage decreases, reactive power is injected into the grid, according to Fig. 1.

Fig. 11 presents the dynamic behaviour of the grid current for the three power control strategies approached. As observed in Fig. 11(a) and (c), APOC and AARC strategies inject unbalanced currents into the grid. On the other hand, BPSC injects balanced current into the grid during voltage sag, as shown in Fig. 11(b). Furthermore, the dynamic saturation scheme implemented guarantees that the output current peak is limited to the rated value, avoiding the system trips due to overcurrent protection. In all cases, the grid currents are sinusoidal and the total harmonic distortion in all cases is lower than 5 %.

The behaviour of instantaneous active and reactive powers is presented in Fig. 12. Double-line frequency oscillations are observed in the reactive power. Regarding the active power, the APOC strategy is able to cancel out the oscillations, as suggested by the theoretical results. Double-line frequency oscillations are observed in the active power for AARC and BPSC strategies. For the case study discussed, AARC results in lower oscillations than BPSC strategy. Furthermore, the average active power injected into the grid is reduced during the voltage sag, due

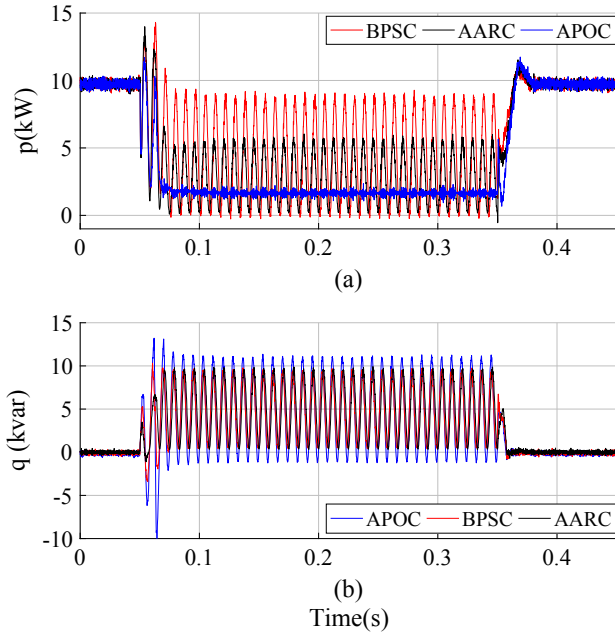


Fig. 12. Dynamic behaviour of instantaneous power delivered to the grid: (a) Active power; (b) Reactive power.

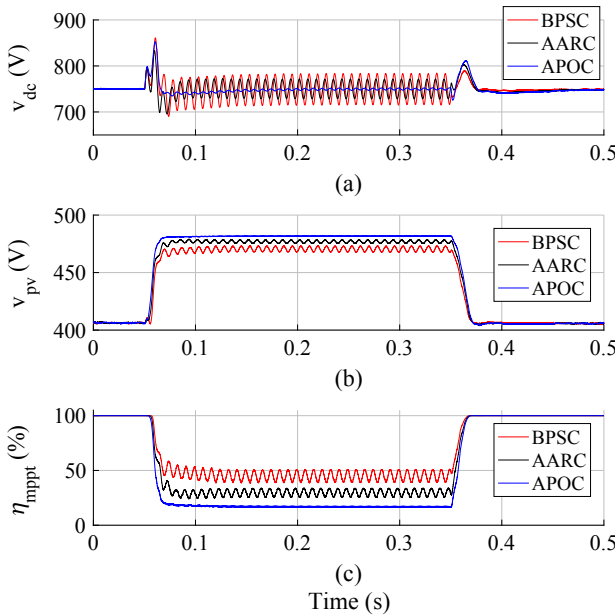


Fig. 13. Dynamic behaviour of the approached power control strategies: (a) Dc-link voltage; (b) PV array voltage; (c) MPPT instantaneous efficiency.

to the dynamic saturation scheme.

The dc-link voltage dynamic behaviour is presented in Fig. 13(a) and this variable presents a similar behaviour of the instantaneous active power. As observed, the double-line frequency voltage oscillations are present for AARC and BPSC. For APOC, these oscillations are strongly attenuated but not completely eliminated, due to the control delay.

The PV array voltage is presented in Fig. 13(b). During normal conditions, this variable follows the MPPT algorithm reference. During the voltage sags, the power curtailment strategy saturates the boost current control loop and the PV array voltage increases, reducing the generated power. The fast transient response is related with the proposed feedforward action. When the voltage sag finishes, the PV array voltage returns to the previous value.

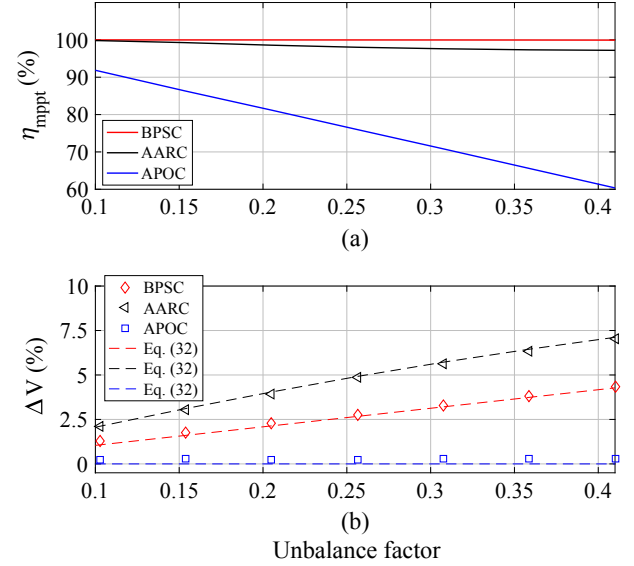


Fig. 14. Comparison of the power control strategies for different unbalance factors for $V^+ = 0.9$ pu: (a) MPPT efficiency; (b) Dc-link voltage ripple.

Regarding the MPPT instantaneous efficiency, shown in Fig. 13(c), the APOC strategy results in the lower efficiency during the voltage sag, resulting in the smallest average active power injection during unbalanced conditions. The double-line frequency oscillations observed in the PV array voltage affects the efficiency. Additionally, for the considered unbalanced voltage sag profile, the BPSC strategy presents the highest MPPT instantaneous efficiency.

6.2. Voltage ripple validation and MPPT efficiency

In order to extend the analysis previously presented, the performance of the power control strategies are evaluated in terms of voltage ripple and MPPT efficiency. Two scenarios are approached. Firstly, an unbalanced voltage profile with 0.9 pu of positive sequence is considered. In the second scenario, an unbalanced voltage profile with 0.6 pu of positive sequence voltage is simulated. The analysis are performed for several values of unbalance factor.

Fig. 14 presents the results for the first scenario. In such conditions, $V^+ = 0.9$ pu. Therefore, according to Fig. 1, $Q^* = 0$. As observed in Fig. 14(a), the MPPT efficiency for BPSC strategy is practically 100 %. Interestingly, AARC strategy presents a slight decrease in the MPPT efficiency with the unbalance factor. For APOC strategy, the efficiency also reduces with the unbalance factor. Additionally, APOC strategy presents the lowest values of MPPT efficiency for any unbalance factor. The reduction in the MPPT efficiency is justified by the negative sequence currents processed by AARC and APOC strategies, which are dependent on the negative sequence voltage. When the unbalance factor is increased, the power curtailment mode is enabled and the converter injects less active power into the grid in order to limit the peak of grid current to the rated conditions. Thereby, the MPPT efficiency reduces.

Fig. 14(b) presents the percentage voltage ripple of the power control strategies. For BPSC strategy the dc-link voltage ripple increases almost linearly with the unbalance factor. This fact is observed because the positive sequence current is constant for this strategy and the energy variation function changes only with the negative sequence voltage, as suggested by relation (39). For AARC the voltage ripple obtained is higher than BPSC strategy. This happens because $Q^* = 0$. In such conditions, the ratio Q^*/P^* is null, and the energy storage requirement of AARC is higher than BPSC, as previously shown in Fig. 6. Finally, the voltage ripple for APOC strategy is very low, since this strategy cancels out the double-line frequency active power oscillation.

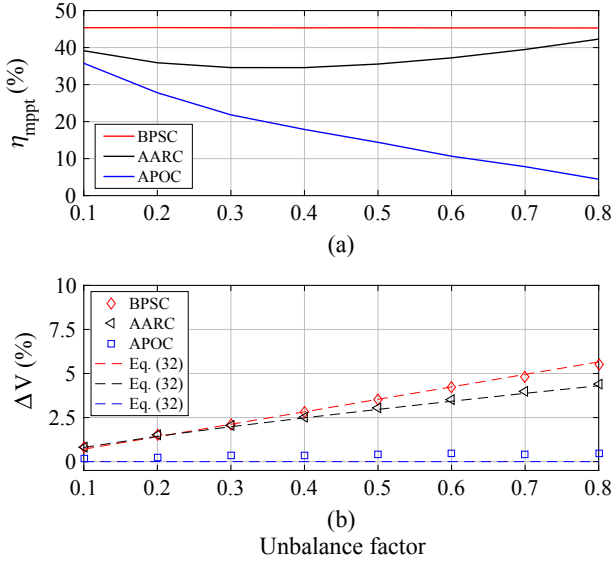


Fig. 15. Comparison of the power control strategies for different unbalance factors for $V^+ = 0.6$ pu: (a) MPPT efficiency; (b) Dc-link voltage ripple.

Fig. 15(a) presents the behaviour of MPPT instantaneous efficiency for the second scenario. As observed, the MPPT efficiency of BPSC strategy is independent of the unbalance factor, once this strategy injects active and reactive power only considering the positive sequence voltage. On the other hand, for APOC strategy the efficiency decreases with the unbalance factor. Finally, for AARC strategy, the efficiency is also strongly dependent of the unbalance factor. Interestingly, AARC strategy presents a decrease with the unbalance factor until $u \approx 0.4$ and an opposite behaviour after this point. As observed, the relation between the unbalance factor and the MPPT efficiency is not straightforward.

Fig. 15(b) presents the percentage voltage ripple of the power control strategies. BPSC strategy presents the higher voltage ripple, which increases almost linearly with the unbalance factor, as previously observed. For AARC, a different behaviour is observed because the positive sequence current is dependent on the unbalance factor while the ratio Q^*/P^* is dependent on the positive sequence voltage component during the sag. Finally, the voltage ripple observed for APOC strategy is very small.

The voltage ripple obtained through the simulations of both scenarios are compared with theoretical values obtained from Eq. (32). As observed in Fig. 14(b) and Fig. 15(b), the theoretical analysis results in a satisfactory capacitor voltage ripple estimation.

6.3. Modern grid codes versus dc-link capacitor stress

The power losses in the dc-link and solar array capacitors are caused by two harmonic groups in the capacitor current. The first group is the second order harmonic component related with the negative sequence voltage of PCC. Furthermore, there are high frequency components originated by the inverter and boost converter switching process. These high frequency components are related with the active power processed by the system.

In order to show this phenomenon, two simulations are implemented and the capacitor current harmonic spectra is evaluated. For simplicity, only BPSC strategy is approached. In the first scenario, a balanced condition is simulated. As shown in Fig. 16(a), the capacitor current presents practically only high frequency components. These components are located around integer multiples of the boost converter and inverter switching frequencies (20 and 12 kHz, respectively). For the second case, the unbalanced voltage sag of Fig. 10 is simulated. As shown in Fig. 16(b), the capacitor current is composed by low and high frequency components. The reduction observed in the high frequency components is justified by the power curtailment strategy, which

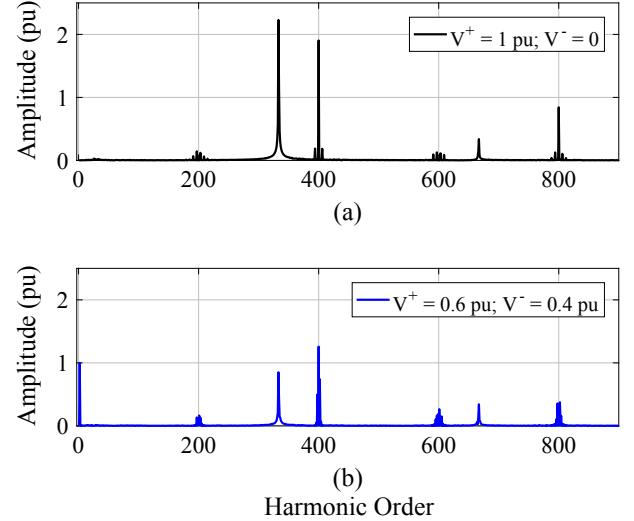


Fig. 16. Comparison of the power control strategies for different unbalance factors: (a) MPPT efficiency; (b) Dc-link voltage ripple.

reduces the active power injection, as previously shown in Fig. 12.

The current spectra presented in Fig. 16 were normalized by the second order component generated in the second case. As observed, the value of high frequency components reduce considerably while the value of low frequency components increase. Additionally, the value of ESR changes with the frequency value, as previously shown in Fig. 8. Thus, even if the amplitude ratio of high and low frequencies is known, it is not straightforward to conclude if the power losses (and temperature) will increase or decrease. Therefore, a more detailed analysis is necessary to find the critical operation point for capacitors in terms of thermal stress. As will be discussed in this section, the GC requirements have a crucial role in the capacitor stress.

It is reasonable to consider that the maximum unbalance factor results in the maximum stress in dc-link. Therefore, it is interesting to determine what is the maximum value of u which guarantees that the amplitude of all phases is limited to V_{max} . Clearly, this value is dependent on the values of φ_v^+ and φ_v^- . It is possible to prove that $\varphi_v^+ - \varphi_v^- = \frac{\pi}{3}$ results in the maximum possible unbalance factor. Using this information, the maximum unbalance factor u_{max} can be calculated by:

$$u_{max} = -\frac{1}{2} + \frac{1}{2} \sqrt{\left(\frac{2V_{max}}{V^+}\right)^2 - 3}. \quad (41)$$

Considering this limit, $\max\{v_a, v_b, v_c\} \leq V_{max}$ is satisfied for any operational condition. Relation (41) is plotted in Fig. 17 for $V_{max} = 1.2$. As observed, the operation points of the inverter are divided in four regions with respect to the injection of active and reactive power. The

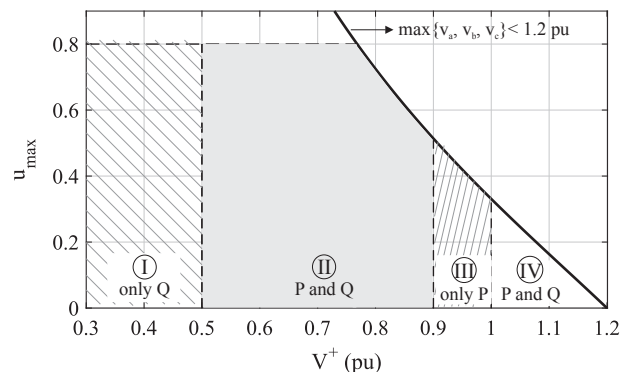


Fig. 17. Maximum possible unbalance factors in the grid as function of the positive sequence voltage.

Table 6
Thermal stresses in the dc-link capacitors.

PSC	T_{hs} (rated)	T_{hs} (Worst case)	Region
BPSC	62.6 °C	66.8 °C	III
AARC	62.6 °C	68.4 °C	III
APOC	62.6 °C	64.3 °C	III

Table 7
Thermal stresses in the solar array capacitors.

PSC	T_{hs} (rated)	T_{hs} (Worst case)	Region
BPSC	42.9 °C	43.2 °C	III
AARC	42.9 °C	43.8 °C	III
APOC	42.9 °C	42.9 °C	III

unbalance factor is limited to 0.8. Based on the facts discussed, the following conclusions can be stated:

- In region (I) the inverter does not process active power and the high frequency components will be strongly reduced. In this case, the losses will be smaller than in balanced conditions even for large unbalance factors;
- In region (II), the inverter will deliver both active and reactive power. In this case, the power curtailment strategy will operate and consequently, the high frequency components will reduce in comparison to the balanced conditions. On the other hand, the contribution of low frequencies increases. Therefore, this region requires analysis;
- Region (III) needs attention for BPSC. The second order harmonic components will be superposed to the high frequency components, which will not be reduced since the efficiency of the MPPT is constant in this region (Fig. 14). In such conditions, this region is critical for BPSC strategy.
- Region IV present the most limited values of unbalance factor and this region will not be critical for the capacitors.

Based on these arguments, the thermal stresses were evaluated for the three power control strategies considering the regions (II) and (III). Basically, the capacitor current harmonic spectra were evaluated for many values of positive sequence and unbalance factor and the hot-spot temperatures where evaluated. For simplicity, only the critical case is presented. The capacitor thermal stresses are compared with the temperature during balanced conditions and rated active power injection.

The thermal stresses in the dc-link and solar array capacitors are shown in Tables 6 and 7, respectively. As observed, the worst operational cases happen in region (III). Furthermore, the dc-link capacitors are more influenced than solar array capacitors since the second order oscillations is more significant in dc-link voltage. The AARC strategy results in the highest thermal stress followed by BPSC strategy. Once APOC strategy cancels out the second order oscillations, the thermal stress during unbalanced conditions is practically the same in steady-state.

7. Conclusions

This work presents a deep discussion regarding power control strategies during unbalanced voltage sags. The three most interesting power control strategies for PV systems were compared in terms of dynamic behaviour, dc-link voltage ripple, MPPT efficiency and thermal stress in the dc-link and solar array capacitors.

Analytical results for the capacitor voltage ripple estimation were derived and validated through simulation results. The mathematical modelling presented is general and can be employed for any power control strategy which can be represented by the FPNPC strategy.

Regarding the capacitor thermal stress, the use of APOC strategy

results in similar thermal stress of rated conditions. Therefore, this strategy has a smaller influence in dc-link capacitor lifetime. AARC strategy reduces the conduction losses in the grid but the stresses in dc-link capacitors increase due to the second order oscillation. Finally, the worst operational scenario in terms of capacitor stress occurs in the dead band of GC curve.

Acknowledgement

The authors would like to thank the Brazilian agencies CNPq, CAPES and FAPEMIG by funding.

Appendix A. Supplementary material

Supplementary data associated with this article can be found, in the online version, at <https://doi.org/10.1016/j.ijepes.2018.10.014>.

References

- [1] de Almeida JOMB, Trres AG, Cupertino AF, Pereira HA. Three-phase photovoltaic inverters during unbalanced voltage sags: comparison of control strategies and thermal stress analysis. In: 2016 12th IEEE International conference on industry applications (INDUSCON); 2016. p. 1–7.
- [2] Teodorescu R, Liserre M, Rodriguez P. Grid converters for photovoltaic and wind power systems. John Wiley & Sons; 2011.
- [3] Camacho A, Castilla M, Miret J, Borrell A, de Vicua LG. Active and reactive power strategies with peak current limitation for distributed generation inverters during unbalanced grid faults. IEEE Trans Ind Electron 2015;62(3):1515–25.
- [4] Afshari E, Moradi GR, Rahimi R, Farhangi B, Yang Y, Blaabjerg F, et al. Control strategy for three-phase grid-connected pv inverters enabling current limitation under unbalanced faults. IEEE Trans Ind Electron 2017;64(11):8908–18.
- [5] Rodriguez P, Timbus A, Teodorescu R, Liserre M, Blaabjerg F. Reactive power control for improving wind turbine system behavior under grid faults. IEEE Trans Power Electron 2009;24(7):1798–801.
- [6] Mirhosseini M, Pou J, Agelidis VG. Single and two-stage inverter-based grid-connected photovoltaic power plants with ride-through capability under grid faults. IEEE Trans Sustain Energy 2015;6(3):1150–9.
- [7] Rodriguez P, Timbus AV, Teodorescu R, Liserre M, Blaabjerg F. Flexible active power control of distributed power generation systems during grid faults. IEEE Trans Ind Electron 2007;54(5):2583–92.
- [8] Castilla M, Miret J, Sosa JL, Matas J, Vicua LGD. Grid-fault control scheme for three-phase photovoltaic inverters with adjustable power quality characteristics. IEEE Trans Power Electron 2010;25(12):2930–40.
- [9] Wang F, Duarte JL, Hendrix MAM. Pliant active and reactive power control for grid-interactive converters under unbalanced voltage dips. IEEE Trans Power Electron 2011;26(5):1511–21. <https://doi.org/10.1109/TPEL.2010.2052289>.
- [10] Chen HC, Lee CT, Cheng PT, Teodorescu R, Blaabjerg F. A low-voltage ride-through technique for grid-connected converters with reduced power transistors stress. IEEE Trans Power Electron 2016;31(12):8562–71.
- [11] Rodriguez P, Medeiros G, Luna A, Cavalcanti MC, Teodorescu R. Safe current injection strategies for a statcom under asymmetrical grid faults. In: 2010 IEEE Energy conversion congress and exposition; 2010. p. 3929–35.
- [12] Nasiri M, Mohammadi R. Peak current limitation for grid side inverter by limited active power in pmsg-based wind turbines during different grid faults. IEEE Trans Sustain Energy 2017;8(1):3–12.
- [13] Pereira HA, Domingos RM, Xavier LS, Cupertino AF, Mendes VF, Paulino JOS. Adaptive saturation for a multifunctional three-phase photovoltaic inverter. In: 2015 17th European conference on power electronics and applications; 2015. p. 1–10.
- [14] Rodriguez P, Teodorescu R, Candela I, Timbus AV, Liserre M, Blaabjerg F. New positive-sequence voltage detector for grid synchronization of power converters under faulty grid conditions. In: 2006 37th IEEE Power electronics specialists conference; 2006. p. 1–7.
- [15] Yepes AG, Freijedo FD, Lopez O, Doval-Gandoy J. Analysis and design of resonant current controllers for voltage-source converters by means of nyquist diagrams and sensitivity function. IEEE Trans Ind Electron 2011;58(11):5231–50.
- [16] Sera D, Teodorescu R, Hantschel J, Knoll M. Optimized maximum power point tracker for fast-changing environmental conditions. IEEE Trans Ind Electron 2008;55(7):2629–37.
- [17] Sera D, Mathe L, Kerekes T, Spataru SV, Teodorescu R. On the perturb-and-observe and incremental conductance MPPT methods for PV systems. IEEE J Photovoltaics 2013;3(3):1070–8.
- [18] Sangwongwanich A, Yang Y, Blaabjerg F, Wang H. Benchmarking of constant power generation strategies for single-phase grid-connected photovoltaic systems. IEEE Trans Ind Appl 2017;PP(99):1.
- [19] Akagi E, Watanabe H, Aredes M. Instantaneous power theory and applications to power conditioning. WileyIEEE Press; 2007.
- [20] Rodriguez P, Luna A, Hermoso JR, Etxeberria-Otadui I, Teodorescu R, Blaabjerg F. Current control method for distributed generation power generation plants under grid fault conditions. In: IECON 2011 - 37th Annual conference of the IEEE industrial electronics society; 2011. p. 1262–9.
- [21] Sharifabadi K, Harnefors L, Nee H, Norrga S, Teodorescu R. Design, control and application of modular multilevel converters for HVDC transmission systems. John Wiley & Sons; 2016. p. 13–5 [Chapter 1].
- [22] Yang Y, Ma K, Wang H, Blaabjerg F. Instantaneous thermal modeling of the DC-link capacitor in photovoltaic systems. In: 2015 IEEE Applied power electronics conference and exposition (APPEC); 2015. p. 2733–9.